A&A 533, A107 (2011)
DOI: 10.1051/0004-6361/200912442

Astronomy & Astrophysics

Structure of the outer layers of cool standard stars⋆

S. Dehaes[1], E. Bauwens[1], L. Decin[1,2,⋆⋆], K. Eriksson[3], G. Raskin[1], B. Butler[4], C. D. Dowell[5], B. Ali[6], and J. A. D. L. Blommaert[1]

[1] Instituut voor Sterrenkunde, Department of Physics and Astronomy, K.U. Leuven, Celestijnenlaan 200D, 3001 Leuven, Belgium
e-mail: Leen.Decin@ster.kuleuven.be
[2] Sterrenkundig Instituut Anton Pannekoek, University of Amsterdam, Kruislaan 403 1098 Amsterdam, The Netherlands
[3] Department of Astronomy and Space Physics, Uppsala University, Box 515, 751 20 Uppsala, Sweden
[4] NRAO PO Box O, Socorro NM, 87801, USA
[5] Jet Propulsion Laboratory / California Institute of Technology, MS 169-506, 4800 Oak Grove Dr., Pasadena, CA 91109, USA
[6] IPAC / Caltech, MS 100-22, Pasadena, CA 91125, USA

Received 7 May 2011 / Accepted 19 April 2011

ABSTRACT

Context. Among late-type red giants, an interesting change occurs in the structure of the outer atmospheric layers as one moves to later spectral types in the Hertzsprung-Russell diagram: a chromosphere is always present, but the coronal emission diminishes and a cool massive wind steps in.
Aims. Where most studies have focussed on short-wavelength observations, this article explores the influence of the chromosphere and the wind on long-wavelength photometric measurements. The goal of this study is to assess wether a set of standard near-infrared calibration sources are fiducial calibrators in the far-infrared, beyond 50 μm.
Methods. The observational spectral energy distributions were compared with the theoretical model predictions for a sample of nine K- and M-giants. The discrepancies found are explained using basic models for flux emission originating in a chromosphere or an ionised wind.
Results. For seven out of nine sample stars, a clear flux excess is detected at (sub)millimetre and/or centimetre wavelengths, while only observational upper limits are obtained for the other two. The precise start of the excess depends upon the star under consideration. For six sources the flux excess starts beyond 210 μm and they can be considered as fiducial calibrators for *Herschel*/PACS (60–210 μm). Out of this sample, four sources show no flux excess in the *Herschel*/SPIRE wavelength range (200–670 μm) and are good calibration sources for this instrument as well. The flux at wavelengths shorter than ∼1 mm is most likely dominated by an optically thick chromosphere, where an optically thick ionised wind is the main flux contributor at longer wavelengths.
Conclusions. Although the optical to mid-infrared spectrum of the studied K- and M-type infrared standard stars is represented well by a radiative equilibrium atmospheric model, a chromosphere and/or ionised stellar wind at higher altitudes dominates the spectrum in the (sub)millimetre and centimetre wavelength ranges. The presence of a flux excess has implications on the role of the stars as fiducial spectrophotometric calibrators in these wavelength ranges.

Key words. stars: chromospheres – stars: late-type – stars: winds, outflows – radio continuum: stars

1. Introduction

Several studies in the past three decades (see, e.g., Linsky & Haisch 1979; Ayres et al. 1981; Hünsch et al. 1996; Haisch et al. 1990) have revealed dividing lines in the cool half of the Hertzsprung-Russell (HR) diagram, where the giants and supergiants reside. These dividing lines are based on differences in the physics of the outer atmospheric layers. On the blue side of the dividing lines, the late-type stars are surrounded by chromospheres and coronae. On the red side the stars also possess chromospheres, but in combination with a cool stellar wind. When introducing the dividing lines (Linsky & Haisch 1979; Ayres et al. 1981), there were no observational indications for a corona on the red side, but nowadays there is evidence of some coronal emission, although much weaker than on the blue side of the dividing lines (Ayres et al. 1997).

Most studies of these outer stellar layers have focussed on X-ray and UV observations. But the far-infrared (FIR) continuum can also be used to probe the outer layers of the atmosphere for solar and cooler stars. As the primary infrared (IR) continuum opacity, coming from free-free processes, increases with the square of wavelength, we see emission from layers that are farther out, the longer the wavelength we observe.

In this study, we use (sub)millimetre and centimetre wavelength observations to gain deeper insight into the outer structure of nine giants of spectral types K and M. The selected stars are 'standard' stars, used in the calibration pedigree of many IR spectroscopic and photometric instruments. All of them belong to the group of stars with no or low coronal activity. With the launch of the ESA-satellite *Herschel*, which covers the full 55 to 672 μm wavelength range, it is of interest to study whether these low-activity stars can also be used as calibrators at these far-infrared wavelengths. In Sect. 2 the selection criteria for the stars are outlined. Data reduction for the different datasets is presented in Sect. 3. Section 4 compares the spectral energy

⋆ Appendix A is available in electronic form at
http://www.aanda.org
⋆⋆ *Postdoctoral Fellow of the Fund for Scientific Research, Flanders.*

Table 1. Some characteristics of the sample stars.

	Spectral type	M_{bol}	$B-V$
α Boo	K2 IIIp	-0.90 ± 0.05	1.23
α Cet	M2 III	-3.09 ± 0.13	1.66
α Tau	K5 III	-1.72 ± 0.06	1.54
β And	M0 III	-3.14 ± 0.11	1.58
β Peg	M2.5 III	-3.34 ± 0.11	1.67
γ Dra	K5 III	-2.07 ± 0.07	1.52
β UMi	K4 III	-1.71 ± 0.07	1.51
ι Aur	K3 II	-2.4	1.55
σ Lib	M3/M4 III	-3.6	1.65

Notes. The values for M_{bol} are taken from Decin et al. (2003a), Kashyap et al. (1994) and Eggen & Stokes (1970). No uncertainties were given in these articles on the values of M_{bol} for ι Aur and σ Lib.

distributions (SEDs) of the stars with atmospheric model predictions. In Sect. 5, the discrepancies found in the previous section are discussed. Section 6 discusses the influence of a corona, chromosphere, or ionised stellar wind on the SEDs. The conclusions are given in Sect. 7.

2. Sample selection

The stars in our sample are part of a larger set of standard stars used for the spectrophotometric calibration of near- and mid-infrared instruments (Decin et al. 2003b,c,a, 2004; Decin & Eriksson 2007; Gordon et al. 2007). They are selected for their brightness in the micrometer and submillimetre wavelength ranges and for their low chromospheric and coronal activity (see, e.g., Wiedemann et al. 1994; Obrien & Lambert 1986, and further in Sects. 6.2 and 6.1). The position of our sample stars in the HR-diagram indeed indicates that they have low coronal activity, however, their positions also points to the possible presence of a cool stellar wind. These stars are potential candidates to be selected as fiducial calibration sources for the PACS (60–210 μm) and SPIRE (200–670 μm) instruments, which are on board the ESA *Herschel*-satellite. Hence, it is necessary to check if the possible chromosphere, corona or stellar wind causes a flux excess in the far-infrared. Some characteristics of the selected stars are given in Table 1.

3. Observations and data reduction

To construct the SEDs of each of the standard stars several photometric data points were gathered from the literature. We have used the UBVRIJKLMNH Photoelectric Catalogue (Morel & Magnenat 1978), the IRAS catalogue of Point Sources (IRAS PSC), Version 2.0 (Beichman et al. 1988), observations in the Geneva Photometric System 4 (Rufener 1989), radio continuum data from Wendker (1995) and Cohen et al. (2005), photometric data in the Johnson's 11-color system (Ducati 2002), the COBE DIRBE Point Source Catalog (Smith et al. 2004), the 2MASS All-Sky Catalog of Point Sources (Skrutskie et al. 2006), IR photometry from the Absolute Calibration Programme for ISO from Cohen et al.[1] and J_n-band photometry from Selby et al. (1988). A summary of the available data can be found in Tables A.1–A.5 in the Appendix.

In order to study the outer atmospheric layers, (sub)millimetre and centimetre data have been obtained with (1.) the SIMBA bolometer array at 1.2 mm at the SEST telescope; (2.) the MAMBO II bolometer array at 1.2 mm on the IRAM telescope; (3.) the SHARC II camera at 350 μm and 450 μm on the CSO; and (4.) the VLA at 22 and 43.3 GHz. The reduction of each of these newly obtained data-sets is briefly discussed in the next paragraphs.

[1] http://iso.esac.esa.int/users/expl_lib/ISO/wwwcal/isoprep/cohen/

Table 2. Fluxes at 1.2 mm determined from SIMBA observations.

Target	Flux (mJy)	Ideal aperture (arcsec)	rms (mJy)
α Boo	105.6 ± 6.9	45	8.4
β And	<40.1		13.8
α Cet	58.3 ± 4.1	55	6.0
β Peg	29.2 ± 2.5	20	6.6

Notes. The ideal aperture is listed in Col. 3, and the rms noise on the sky background in Col. 4. The given uncertainty does not take the uncertainty on the absolute flux calibration into account.

3.1. SIMBA observations

α Boo, β And, α Cet and β Peg were observed with SIMBA (2003 July 13–15) at 1.2 mm, using the fast-scanning technique. The MOPSI[2] software developed by R. Zylka was used for the data reduction. In a first reduction step, some fundamental operations like despiking, opacity correction and sky-noise reduction are performed on each scan. Once the scans made during different nights are assembled, the position of the source is more accurately determined, which can be used for baseline definition and for improvement of the sky-noise reduction. For the absolute calibration, scans of Uranus were used. The model for Uranus is the standard model offered by MOPSI, the calibration uncertainties are estimated at 15%. After the data reduction, fluxes were determined using aperture photometry. For each source, the "ideal" aperture was determined, being the aperture with the highest corresponding signal-to-noise ratio. A more vast description of the data reduction and analysis of the SIMBA data is given in Dehaes et al. (2007). Table 2 shows the determined fluxes together with the ideal aperture used and the rms noise on the sky background.

3.2. MAMBO II observations

Observations at 1.2 mm with MAMBO II were obtained for α Boo, ι Aur, β UMi, γ Dra, α Tau, β And, α Cet, β Peg and σ Lib (2003 October-November). The reduction was done with an adjusted version of the MOPSI software called MOPSIC[3]. These scripts also include standard reduction steps such as baseline fitting, despiking, correlated skynoise filtering, etc. Flux calibration is done using a default conversion factor provided by MOPSIC, the calibration uncertainties are estimated at 15%. After these reduction steps, scans of the same source are combined to give one result. Table 3 lists the determined fluxes.

For four sources both SEST and IRAM data were available. Both measurements coincide for β Peg and the upper limit determined from the SIMBA observations is in agreement with the flux measured by MAMBO II for β And. For α Boo and α Cet, the two measurements do not agree within the errors. As the MAMBO II observations were performed in service mode and the log-files state very unstable weather conditions for α Cet and

[2] Observers Handbook SIMBA, 2003, edition 1.9, http://www.ls.eso.org/lasilla/Telescopes/SEST/html/telescope-instruments/simba/index.html

[3] http://www.iram.es/IRAMES/mainWiki/CookbookMopsic

Table 3. Fluxes at 1.2 mm determined from MAMBO II observations.

Target	Flux (mJy)
α Boo	[20.8 ± 3.5]
ι Aur	5.5 ± 1.6
β UMi	12.2 ± 1.6
γ Dra	10.1 ± 1.3
β And	23.5 ± 2.7
α Cet	[23.6 ± 2.5]
β Peg	29.5 ± 3.2
σ Lib	12.1 ± 2.0

Notes. α Tau is not listed here, since the uncertainty on the measurement was too large to give any restraints. The observations of α Boo and α Cet are discarded in the subsequent analysis (see Sect. 3.2 for explanation).

altocumulus clouds right after the observation of α Boo, we have more confidence in the results from the SIMBA observations (which were performed in visitor mode). For α Boo and α Cet the MAMBO II observations are discarded for the remainder of the article. Since the MAMBO II observations for the other objects are in good agreement with the SIMBA data (e.g. β Peg), with data from the catalogues (e.g. β And) and since measurements at these long wavelengths are scarce, the data are retained for the other objects.

3.3. CSO observations

Observations of five giant stars were made at 350 μm and 450 μm using the SHARC II camera at Caltech Submillimetre Observatory on several nights in 2005 and 2008. Standard Lissajous scans were used for the stars and calibrators. The weather conditions were favourable: clear skies, low humidity, and precipitable water vapour in the range 1−2 mm. Occasional periods of unstable atmospheric transmission appear to have been properly accounted for in the data analysis. Instead of using the facility 225 GHz radiometer for atmospheric extinction correction, we used (for each observation in Table 4) the tight correlation between the observed signals from the calibrators (in raw V) and the average full DC voltage of the bolometers at the time of the observations to calculate a calibration factor which was then applied to the target star. The full DC bolometer voltage is responsive to the emission from the atmosphere and therefore its transparency. In the analysis, the detectors were corrected for their slight nonlinear response. The beam size of CSO/SHARC II at 350 and 450 μm is 8.3 ± 0.3 arcsec and 9.8 ± 0.3 arcsec, respectively, and all of the giant stars are unresolved. The calibrators are unresolved or only slightly resolved.

The absolute flux calibration is based on the Wright (1976) model for Mars and subsequent planet observations and analysis by Griffin & Orton (1993). From this work, the absolute uncertainties in the fluxes of Uranus and Neptune are believed to be 5%. Our submillimetre observations of β Peg are calibrated directly vs. Uranus and Neptune and are assigned a systematic calibration uncertainty of 10 % in Table 4. For the remaining sources, we used secondary calibrators having fluxes tabulated by Sandell (1994), Sandell (priv. comm.), Jenness et al. (2002), the JCMT/SCUBA flux calibration web site (2005 update), and our own cross calibration work. Our best estimates for the secondary calibrator fluxes are given in the table, and the target stars calibrated with respect to them are assigned a systematic uncertainty of 15%. In several cases, the statistical uncertainties are much smaller than the systematic uncertainties, so these measurements would benefit from an improved knowledge of the fluxes of the secondary calibrators.

3.4. VLA observations

The VLA (Very Large Array) measurements were taken at two wavelengths: 0.7 cm (Q-band) and 1.3 cm (K-band). In all of our observations, we observed in the continuum mode, which provides measurements of the total intensity (Stokes I) with a bandwidth of ∼92 MHz. The observations for α Boo were undertaken on two separate occasions (January 6, 1999, and January 25, 2004), for β Peg on April 21, 2005. For the 1999 experiment, the VLA was in the C configuration, with maximum physical antenna separation of ∼3.4 km. At this time, only about half of the antennas were equipped with Q-band receivers and during our experiment 12 were available for this frequency. The other 15 were tuned to K-band for simultaneous observations. The α Boo observations were part of a larger program to observe possible sources for millimetre wavelength flux calibration that time, and as such were limited to only about an hour in extent. For the 2004 and 2005 experiments, the VLA was in the B configuration, with maximum physical antenna separation of ∼11.4 km. A full 6 h observation was dedicated to the star at Q-band.

Subsequent calibration of the data proceeded in the normal fashion for VLA data, in the AIPS reduction package (http://www.cv.nrao.edu/aips/). For all data, the absolute flux density scale was set with an observation of 3C286, with assumed flux densities of 1.455 and 2.520 Jy for Q- and K-bands, respectively. Uncertainties in this flux density scale are ∼10% at Q-band and 5% at K-band. Observations of the unresolved secondary calibrator J1357+193 were used to remove long timescale (minutes) atmospheric and system fluctuations in the data. The derived flux densities of J1357+193 were 0.668 and 0.835 Jy at Q- and K-bands in 1999, and 1.175 Jy at Q-band in 2004 (the level of variation is common with these point-like calibration QSOs at radio wavelengths).

Images were then constructed from the visibilities via standard AIPS routines. The images were lightly CLEANed (a few 10's of components) to remove the sampling pattern of the array from them. The final total flux density was then calculated in five different ways: (1.) by counting up the flux density in the CLEAN components; (2.) by taking the peak flux density in the image; (3.) by counting up the flux density around the central location in the image; (4.) by fitting a gaussian to the image, and taking the peak of that fit gaussian (we do not actually resolve the star); and (5.) by actually fitting the visibilities themselves to find the flux density of a point source near the image center. The final estimated flux density is taken as the median of these five estimates. The uncertainty is taken as the average of the uncertainty from the image and visibility fits. This is only the formal uncertainty, systematic uncertainties must be considered in addition to this. These can arise from: inaccurate flux density scale, bad pointing, bad elevation corrections, atmospheric decorrelation, other electronics sources. Of these, by far the dominant uncertainty is the flux density scale, as the others are accounted for in various ways in the calibration.

Table 5 shows the resultant flux densities and uncertainties (formal only) for the VLA observations. The two observations of α Boo at Q-band are consistent with each other, and the K-band observation in 1999 is also consistent, given the expected spectral index.

4. Comparison between SED and theoretical predictions

For wavelengths shortward of 200 μm, the observational SEDs are compared with the theoretical predictions of the SOSMARCS

Table 4. CSO observations at 350 μm and 450 μm.

Star	Wavelength (μm)	Flux (mJy)	Statistical uncertainty (mJy)	Systematic uncertainty (mJy)	Observing dates	Calibrator fluxes (Jy/beam)
α Boo	350	601	35		2005 May 10–13	Arp 220 (10.5)
		538	53		2008 Mar. 1	Arp 220 (10.5)
		507	19		2008 May 28	Arp 220 (10.5)
		529	27	79	average	
α Boo	450	488	48		2008 Mar. 2	Arp 220 (5.4)
		440	11		2008 Apr. 7	Arp 220 (5.4)
		442	11	66	average	
α Cet	350	210	16	32	2008 Sep. 22	Vesta (11.3)
α Cet	450	110	28	17	2008 Sep. 24	Vesta (7.1)
α Tau	350	530	20	80	2008 Sep. 17, 18	Vesta (10.8), Pallas (9.5)
α Tau	450	304	39	46	2008 Sep. 24	Vesta (7.2), CRL 618 (11.8), HL Tau (10.4)
β Peg	350	361	9	36	2008 Sep. 22	Uranus (234), Neptune (92), CRL 2688 (49)
β Peg	450	240	12	24	2008 Sep. 23, 24	Uranus (169), CRL 2688 (26.8)
γ Dra	350	116	25	17	2008 Sep. 22–24	CRL 2688 (49)

Table 5. Final flux densities from VLA observations of α Boo and β Peg.

Target	Date	Frequency GHz	Wavelength cm	Flux density mJy
α Boo	1999-Jan.-06	22.46	1.3	1.7 ± 0.2
α Boo	1999-Jan.-06	43.30	0.7	3.3 ± 0.4
α Boo	2004-Jan.-25	43.30	0.7	3.34 ± 0.08
β Peg	2005-Apr.-21	43.30	0.7	2.49 ± 0.12

Notes. The given uncertainty does not take the uncertainty on the absolute calibration into account.

code of Plez et al. (1992), which is a refined version of the original MARCS code of Gustafsson et al. (1975). The synthetic spectra were computed with TURBOSPECTRUM (Plez et al. 1992), the improved version of the SPECTRUM program. For an overview of the continuum and line opacity lists used, we refer to Decin (2000). The MARCS model atmosphere code is built on the assumptions of local thermodynamic equilibrium, spherical or plane-parallel stratification in homogeneous stationary layers and hydrostatic equilibrium.

For the simulations, the geometry of the radiation transfer problem for the K- and M-giants in our sample was taken to be spherically symmetric. The input parameters for the MARCS models were taken from Decin et al. (2003a) unless indicated otherwise in Table 6. In the same article a discussion about the uncertainties on these parameters can be found. The models were reddened according to the value of the interstellar extinction derived from the model of Arenou et al. (1992) using the distances from Decin et al. (2003a) or Ochsenbein & Halbwachs (1999). The values of the interstellar extinction and the distances are listed in Table 6.

Inhomogeneities in the outer layers make a computation of the model atmosphere structure and theoretical spectrum beyond 200 μm highly unreliable. But, the far-infrared continuum flux beyond 200 μm can be estimated from the theoretical spectrum calculations between 50 and 200 μm. We therefore have determined the temperature of the flux forming region where $\tau_\lambda = 1$, with λ ranging from 50 to 200 μm. With H^- free-free being the main continuum opacity source, subsequent shallower cooler layers are sampled for larger wavelength points. Since H^- shows a power-law behaviour for wavelengths beyond 1 μm (see Bell & Berrington 1987), the temperature for the continuum forming layer at wavelengths beyond 200 μm is estimated from a logaritmic extrapolation of the $T(\tau_\lambda = 1)$-values between 50 and 200 μm (see Fig. 1). The continuum flux at each far-infrared wavelength point is then approximated by the blackbody flux at the characteristic temperature $B_\lambda(T)$ scaled with the appropriate angular diameter. Since we are in the Rayleigh-Jeans part of the spectrum, the flux value is quite insensitive to the temperature, i.e. $\partial B_\lambda(T)/\partial T$ is small.

The accuracy and resolution of today's FIR instruments remain currently too poor to constrain the importance of line veiling in the (sub)millimetre range. The study by Decin & Eriksson (2007) and B. Plez in case of the 40–66 μm spectrum for α Tau (priv. comm.) shows that molecular line absorption at a resolution of ~1500 is typically less than 1% beyond 150 μm. We therefore will compare the (sub)millimetre observational data with *continuum* flux predictions.

The angular diameters (see Table 6) are computed from Selby K-band photometry. For β UMi, we have used the Johnson K-band magnitude of −1.39 (Ducati 2002), yielding a magnitude of −1.45 in the Selby system. Zeropoints are calculated using the Kurucz theoretical spectrum of Vega (Cohen et al. 1992), taking into account the observed near-IR excess of Vega (Absil et al. 2006). For the Selby photometric system we obtain a zeropoint of 4.0517×10^{-10} W/m^2/μm. For all targets, except β UMi and β Peg, an uncertainty of 0.01 mag in the K-band photometric data is propagated in the computation of the uncertainty on the angular diameter. For β UMi the photometric uncertainty is 0.1 mag, while for β Peg we take into account that this target is a low-amplitude variable star in the K-band with an amplitude of 0.03 ± 0.01 mag (Smith et al. 2004).

Figure 2 shows the photometric data in comparison with the theoretical model predictions[4]. For all targets, the theoretical

[4] The MARCS model atmosphere spectra as well as the extrapolation beyond 200 μm, are made available for all targets through the online CDS database. The data are accompanied by a description of the parameters and the absolute calibration used. The dataset made available also includes the model for Sirius, being a A1V stellar calibrator. The parameters used to derive the Sirius model are from Decin et al. (2003c) and the TCS K-band magnitude of –1.388 (Cohen et al. 1999) is used for the absolute calibration.

Table 6. Input parameters for the MARCS code from Decin et al. (2003a) unless indicated otherwise.

	α Boo	ι Aur	β UMi	γ Dra	α Tau
Sp. Type	K2 IIIp	K3 II	K4 III	K5 III	K5 III
$T_{\rm eff}$	4320 ± 140	4160 ± 130[1]	4085 ± 140	3960 ± 140	3850 ± 140
log g	1.5 ± 0.15	1.74 ± 0.36[1]	1.6 ± 0.02	1.30 ± 0.25	1.50 ± 0.15
$\xi_{\rm t}$	1.7 ± 0.5	3.00 ± 0.5[1]	2 ± 0.5	2.0 ± 0.5	1.7 ± 0.5
[Fe/H]	−0.50 ± 0.20	−0.11 ± 0.22[1]	−0.15 ± 0.2	0.00 ± 0.20	−0.15 ± 0.20
ϵ(C)	7.96 ± 0.20	*8.35*	8.25 ± 0.2	8.15 ± 0.25	8.35 ± 0.20
ϵ(N)	7.61 ± 0.25	*8.35*	8.16 ± 0.25	8.26 ± 0.25	8.35 ± 0.25
ϵ(O)	8.68 ± 0.20	*8.93*	8.83 ± 0.2	8.93 ± 0.20	8.93 ± 0.20
^{12}C/^{13}C	7 ± 2	*10*	9 ± 2	10 ± 2	10 ± 2
$\theta_{\rm d}$	20.74 ± 0.10	7.05 ± 0.03	10.15 ± 0.42	9.94 ± 0.05	20.89 ± 0.10
distance	11.26 ± 0.09	166.56 ± 33.31[5]	39.87 ± 7.97[5]	45.25 ± 0.94	19.96 ± 0.38
M_g	0.73 ± 0.27	3.6	2.49 ± 0.92	1.72 ± 1.02	2.30 ± 0.85
$A_{\rm v}$	0.01 ± 0.15	0.00 ± 0.15	0.00 ± 0.5	0.03 ± 0.15	0.03 ± 0.15
K	–3.07[6]	–0.686[6]	-1.45[7]	–1.370[6]	–2.940[6]
	β And	α Cet	β Peg	σ Lib	
Sp. Type	M0 III	M2 III	M2.5 III	M3/M4 III	
$T_{\rm eff}$	3880 ± 140	3740 ± 140	3600 ± 300	3634 ± 110[2]	
log g	0.95 ± 0.25	0.95 ± 0.25	0.65 ± 0.40	0.9 ± 0.31 [2]	
$\xi_{\rm t}$	2.0 ± 0.5	2.3 ± 0.5	2.0 ± 0.3	3.1 ± 0.5[3]	
[Fe/H]	0.00 ± 0.30	0.00 ± 0.30	0.00	*0.00*	
ϵ(C)	8.12 ± 0.30	8.20 ± 0.30	8.20 ± 0.40	8.23 ± 0.04[3]	
ϵ(N)	8.37 ± 0.40	8.26 ± 0.40	8.18 ± 0.40	8.15 ± 0.05[4]	
ϵ(O)	9.08 ± 0.30	8.93 ± 0.30	8.93 ± 0.40	*8.93*	
^{12}C/^{13}C	9 ± 2	10 ± 2	5 ± 3	*10*	
$\theta_{\rm d}$	13.03 ± 0.06	12.34 ± 0.06	16.43 ± 0.24	11.00 ± 0.05	
distance	61.12 ± 2.84	67.48 ± 3.78	61.08 ± 2.69	90.80 ± 18.16[5]	
M_g	2.49 ± 1.48	2.69 ± 1.61	$1.94^{+4.27}_{-1.34}$	1.5	
$A_{\rm v}$	0.06 ± 0.15	0.06 ± 0.16	0.03 ± 0.15	0.20 ± 0.17	
K	–1.930[6]	–1.760[6]	–2.330[6]	–1.471[6]	

Notes. The parameters are the effective temperature $T_{\rm eff}$ in K, the gravity log g in cm/s^2, the microturbulent velocity $\xi_{\rm t}$ in km s^{-1}, the metallicity [Fe/H], the abundances of carbon, nitrogen, and oxygen, the ^{12}C/^{13}C-ratio and the photospheric stellar angular diameter $\theta_{\rm d}$ in milliarcseconds. The calculation of the angular diameter is discussed in Sect. 4. The table also contains the distances (in pc) and the values of the interstellar extinction $A_{\rm v}$ as derived from the model of Arenou et al. (1992) and the K-band magnitude used for the absolute calibration of the SEDs. Values, for which no literature values have been found, have been assumed on the basis of analogue objects, and are listed in italics.
[1] McWilliam (1990), [2] Judge & Stencel (1991); [3] Tsuji (1991); [4] Aoki & Tsuji (1997); [5] Ochsenbein & Halbwachs (1999); [6] Selby et al. (1988); [7] Ducati (2002) scaled to Selby et al. (1988).

predictions underestimate the observations in the millimetre and/or centimetre wavelength area. Where an excess is detectable at 1.2 mm, the model underestimates the observations by an average of 25%. At centimetre wavelengths, the discrepancy amounts to an average of 90%. In the following section, different causes for this excess are explored.

5. Discussion

5.1. Proof for a significant flux excess at 1.2 mm

Figure 2 shows clear indications for a flux excess at millimetre and centimetre wavelengths. To prove the flux excess, both the observational and theoretical uncertainties in the atmosphere models should first be investigated.

Observational uncertainties. The uncertainties on the observations in the millimetre/centimetre wavelength region are typically of the order of 15%. The IRAS-PSC error bars given in the catalogue are the statistical 1σ uncertainty values; realistic absolute calibration uncertainties are lacking for the PSC, but are estimated to be ~20% (D. Kester, priv. comm.).

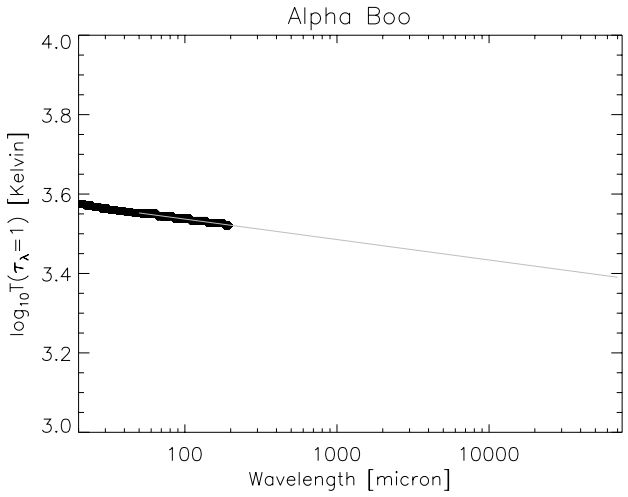

Fig. 1. Temperature of the continuum atmospheric model layer where $\tau_\lambda = 1$ for wavelengths between 20 and 200 μm (black thick symbols) for α Boo. The temperature of the characteristic layer where most of the photospheric flux is formed ($T_{\tau_\lambda=1}$) for the full 200 to 7500 μm wavelength range is derived by extrapolation from the 50 to 200 μm wavelength range (grey line).

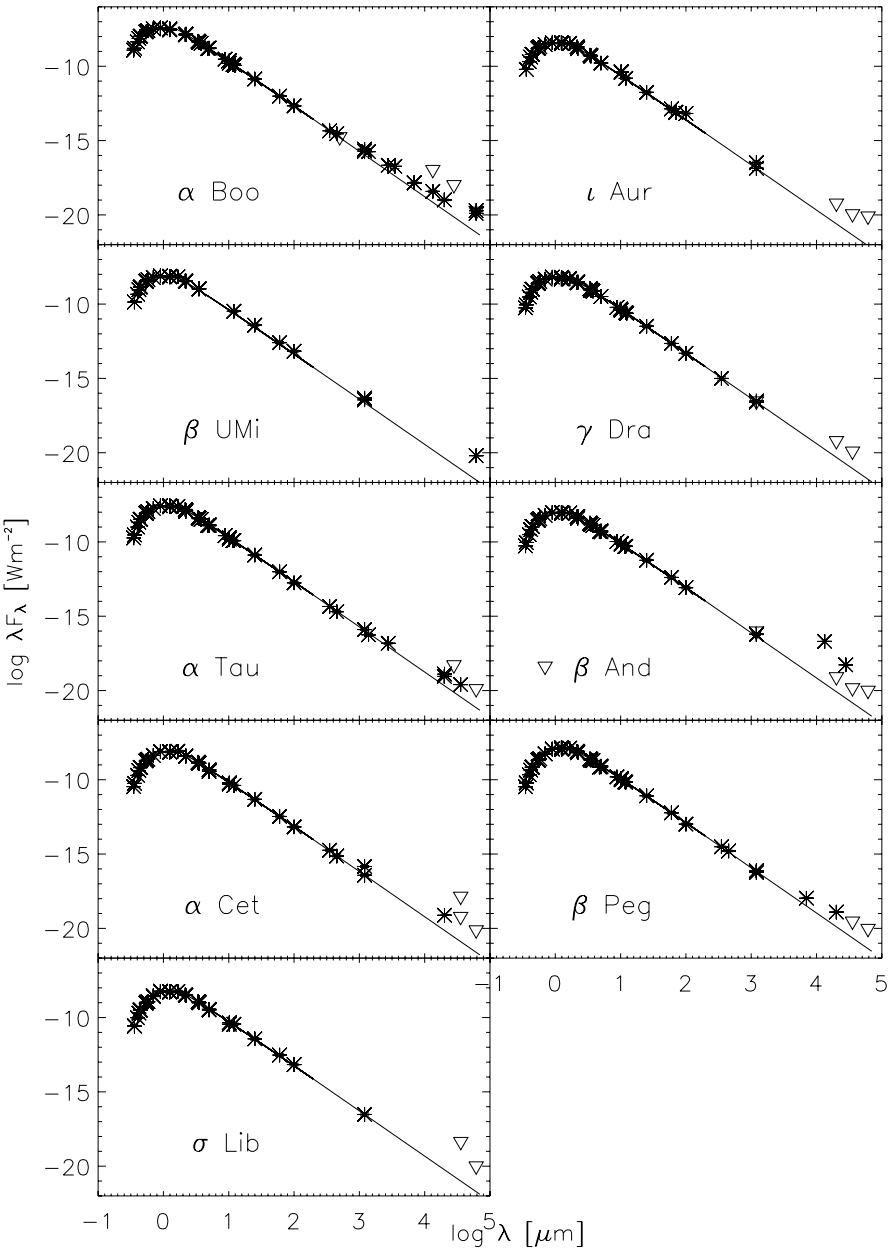

Fig. 2. Comparison between the photometric data (asterisks) and the continuum theoretical spectrum (full line) for the nine sample stars. If several observations are available at the same wavelength, only the maximum and minimum flux value were plotted, except at (sub)millimetre and centimetre wavelengths as this wavelength region is of particular interest here. Most of the error bars fall within the symbols for the data. A reversed triangle represents an upper limit.

This higher uncertainty was already clear from a comparison between the Infrared Space Observatory – Short Wavelength Spectrometer (ISO-SWS) data and the IRAS-PSC and IRAS-LRS data (Van Malderen et al. 2004). Therefore we have used an error bar of 20% on the IRAS-PSC data in our analysis. The IRAS-PSC fluxes are colour corrected. The uncertainties on the near- and mid infrared photometry were taken from the catalogs mentioned in Sect. 3.

Theoretical uncertainties. As described in Decin & Eriksson (2007), the uncertainty on the FIR continuum flux predictions mainly arise from uncertainties on (1) the estimated stellar temperature; and (2) the neglect of some physical processes.

(1) In the FIR, the dominant continuous opacity arises from H^- free-free absorption, whose absorption coefficients are nowadays known at an accuracy of about 1% for wavelengths beyond 0.5 μm over the temperature range between 1000 and 10 000 K (Decin & Eriksson 2007). An uncertainty in the estimated stellar temperature may give rise to an uncertainty on the continuum predictions of up to 4% for A-M giants.

(2) Since we are tracing regions high up in the atmosphere, density inhomogeneities and patchy temperature structures may occur. This kind of 3-dimensional structures are not dealt with in the 1-dimensional MARCS model atmosphere code. Luckily, the continuum extrapolations occur in the FIR, where the sensitivity of the Planck function to the temperature is small. Another important physical process not included in the MARCS atmosphere code is the presence of circumstellar dust and/or a chromosphere or ionised wind. While the latter is the topic of this study, the first excess can be excluded from the detailed analysis of the ISO-SWS data for 7 targets in our sample (Decin et al. 2003a; Van Malderen et al. 2004). ι Aur and σ Lib were not observed by ISO,

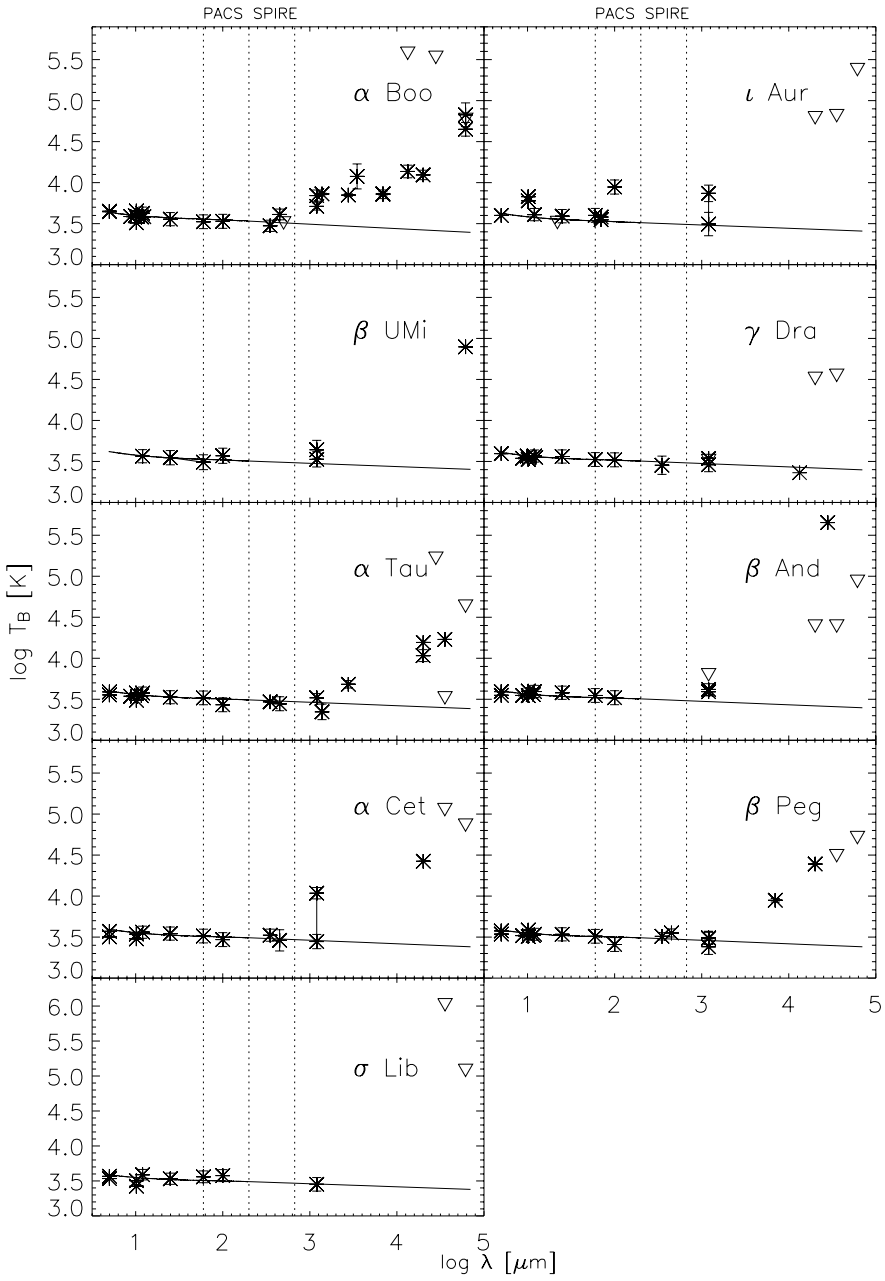

Fig. 3. Brightness temperature T_B in function of the wavelength for the nine sample stars between 5 μm and 7 cm. The full line indicates the brightness temperatures derived from the theoretical model, the asterisks show the brightness temperatures derived from the observations. A reversed triangle represents an upper limit. The error bars on the observational data take the uncertainty on the observations and on the angular diameter into account. The PACS and SPIRE wavelength ranges are indicated by a dotted line, to facilitate comparison to the wavelength region were a flux excess is seen.

but good-quality IRAS-LRS data exist for both objects. The IRAS-LRS data show no sign of flux excess due to circumstellar dust.

A remark concerning the angular diameters that were used to compute the fundamental parameters for the MARCS models is in place here.

At every wavelength, the observed angular diameter represents the apparent diameter of the stellar surface where $\tau_\lambda \sim 1$. Since at the longer wavelengths, we are tracing layers that lie further outwards, it is expected that the angular diameter increases with increasing wavelength. If the angular diameter in the millimetre and centimetre area is considerably larger than the assumed value, the continuum predictions will underestimate the flux in this wavelength region.

To investigate this, we derived the change in height of the continuum forming layers with increasing wavelength for the M0 giant β And. The layer where $\tau_{\rm ross} = 1$ (with $\tau_{\rm ross}$ the Rosseland optical depth) defines the stellar radius, being in case of β And $R_* = 6.12 \times 10^{12}$ cm. The flux at 100 μm is formed at $R_* + 6.90 \times 10^{10}$ cm, for 150 μm at $R_* + 7.89 \times 10^{10}$ cm and for 200 μm at $R_* + 1.70 \times 10^{11}$ cm. From the theoretical model, we derive that the flux at 7 cm is formed at $R_* + 2.23 \times 10^{11}$ cm, which corresponds to an increase in radius of 3.64%. For the other sample stars, comparable numbers are found. This increase in angular diameter is insufficient to explain the observed excess.

In general, the uncertainties on the theoretical flux predictions are in the order of 5 to 10%, excluding the effects of a chromosphere or ionised wind. The observed flux excesses are hence not caused by inaccuracies in the modelling, but are due to physical processes in the stars.

5.2. Brightness temperature

Figure 3 provides another window at studying the flux excess. It shows the brightness temperature over the full 5 μm to 7 cm wavelength range. The brightness temperature is defined as the

temperature of a black body that gives the same flux as the model atmosphere at the indicated wavelength, and can be written as (Cohen et al. 2005)

$$T_{\rm B}(\lambda) = \frac{14387.75/\lambda}{\ln\left(1 + \frac{733.4090\,\theta_{\rm D}^2}{F_\nu(\lambda)\lambda^3}\right)}, \quad (1)$$

where F_ν is the observed flux in Jy, $\theta_{\rm D}$ the angular diameter in milliarcseconds, λ the wavelength in μm, and $T_{\rm B}(\lambda)$ the brightness temperature in K. The uncertainty on the data and on the angular diameter (see previous section) has been propagated to determine the error bars on the observational brightness temperatures. In the approximation for long wavelengths, the formula for the brightness temperature shows that $T_{\rm B}$ is inversely proportional to the angular diameter. Since the angular diameters at long wavelengths might be underestimated when an extra component besides the photosphere is present, the brightness temperatures in Fig. 3 should be regarded as upper limits.

In Fig. 3 one can clearly see the wavelength region where the flux excess starts for each of the sample stars. For ι Aur, the observation at 60 μm still agrees with the model within the error. Also the IRAS-LRS data of ι Aur agree with the model predictions. The flux at 100 μm is in excess of the model. Recently a weak IR flux excess at 70 μm has been found in the Spitzer-MIPS data (Gordon et al. 2007), suggesting that the excess starts between 60 μm and 100 μm. For α Boo, the model and the data coincide for wavelengths up until 350 μm. The measurement at 450 μm lies above the model prediction and the data at longer wavelengths are all clearly in excess of the predictions. For α Cet the excess seems to start between 450 μm and 1.2 mm, as the average flux at 1.2 mm lies well above the model. For β And it starts between 100 μm and 1.2 mm; unluckily no measurements are available between 100 μm and 1.2 mm. For α Tau, β UMi and β Peg, the excess starts at longer wavelengths, as the fluxes until 1.38 mm (respectively 1.2 mm) are still in accordance with the predictions. For γ Dra and σ Lib all available data coincide with the model predictions, including the measurements at 1.2 mm. However, there are no observational data at longer wavelengths and the upper limits at centimetre wavelengths are such that they do not exclude an excess. From this we conclude that α Boo, α Cet, α Tau, β Peg, β UMi, γ Dra, and σ Lib are good calibrators for the PACS photometer (60–210 μm). Recently Poglitsch et al. (2010) have shown that an independent absolute flux calibration based on thermophysical models for a set of asteroids for the PACS photometer, agree very well (better than 5%) in all bands and over a large flux range, with the predicted absolute flux values we obtained for the sources termed as fiducial IR calibrators in previous paragraph.

While this first observational part of this paper already fulfills our goals to assess the reliability of near-infrared K- and M-type standard stars as fiducial far-infrared calibrators, it remains interesting to study the physical causes for the detected far-infrared flux excess. It was already argued that the increase in angular diameter at longer wavelengths does not lead to significant changes in the theoretical model predictions. However, possible extra components not taken into account by the theoretical models, such as a chromosphere, can create excess emission in the far-infrared. Proof for this kind of extension can be found in, for example, Drake & Linsky (1986). They studied observations at 2 and 6 cm of, a.o., α Boo. They treated the radiation at radio wavelengths as originating from an optically thick ionised wind (see also Sect. 6.3), for which they calculated the half-power radius (meaning that half of the radio emission originates from within this radius). For α Boo this half-power radius at 2 cm corresponds to the stellar radius, but at 6 cm this radius had increased to $\simeq$1.7 R_*. In the Sect. 6, we will elaborate on the possibility that the flux excess arises from the presence of a chromosphere (corona) or from thermal emission in an ionised stellar wind.

6. Influence of a chromosphere, corona or ionised stellar wind on the SED

6.1. Influence of a chromosphere at NIR wavelengths

In 1994, Wiedemann et al. studied the fundamental vibration-rotation lines of CO (at ~4.6 μm) in a set of late-type stars. The CO $\Delta v = 1$ lines are remote sensors for the thermal conditions in the outermost layers of the atmosphere. In particular, the strongest CO $\Delta v = 1$ lines occur at or above the temperature minimum in chromospheric solar and stellar models. Wiedemann et al. (1994) interpreted the CO observations in terms of a "thermal bifurcation" model for the atmospheres of their sample stars. It consists of two distinct physical phases that co-exist at chromospheric altitudes. One component is controlled by molecular cooling and is represented by a radiative equilibrium model atmosphere with CO induced temperature depression. The second component is chromosphere and features a temperature inversion produced by the deposition of mechanical energy. Any observed spectrum from an atmosphere with thermal bifurcation is to be interpreted as a spatial sum over the two types of thermal regions with appropriate geometrical weighting factors. For completeness, we want to point out that several objections to the theory of thermal bifurcation have been raised, e.g. Mauas et al. (1990) and Wedemeyer-Böhm & Steffen (2007).

Wiedemann et al. (1994) concluded that the observed infrared CO $\Delta v = 1$ spectrum at 4.6 μm of one group of stars, containing α Boo, α Tau and γ Dra, is well described by homogeneous radiative equilibrium models. The near-IR CO spectra for this group of so-called "quiet" stars indicate that the cool regions dominate the stellar surface for heights between $\sim 10^{-1/2}$ and 10^{-2} g/cm^2 in mass column density, and have large filling factors. These stars are said to have a "COmosphere". For a second group of stars, the CO $\Delta v = 1$ spectrum is poorly represented by radiative equilibrium models, and is compatible with a chromosphere covering the stellar surface homogeneously at these altitudes. After investigation of different chromospheric indicators, it also became clear that the stars in the first group show only little chromospheric activity.

Three stars from our sample, α Boo, α Tau and γ Dra, belong to the first group of "quiet stars" i.e. their CO $\Delta v = 1$ spectrum indicates that the COmosphere dominates the thermal structure at heights between $\sim 10^{-1/2}$ and 10^{-2} g/cm^2 in mass column density. For these stars, the spectrum at NIR wavelengths is not influenced by their chromospheric activity. In the following sections, we investigate if this remains true at longer wavelengths.

6.2. Coronal, transition region and wind dividing lines

Linsky & Haisch (1979) introduced a dividing line (further denoted by DL) in the cool part of the HR diagram on the basis of ultra-violet spectra of late-type stars. Stars to the blue side of the "transition region DL" were termed "solar-type", as they showed spectral lines formed at temperatures of 5×10^3–2×10^5 K, indicative of chromospheres, transition regions and by implication unseen coronae at even hotter temperatures. Stars to the red side are of "non-solar type": they only exhibited lines formed at temperatures below 10 000–20 000 K, indicative of chromospheres

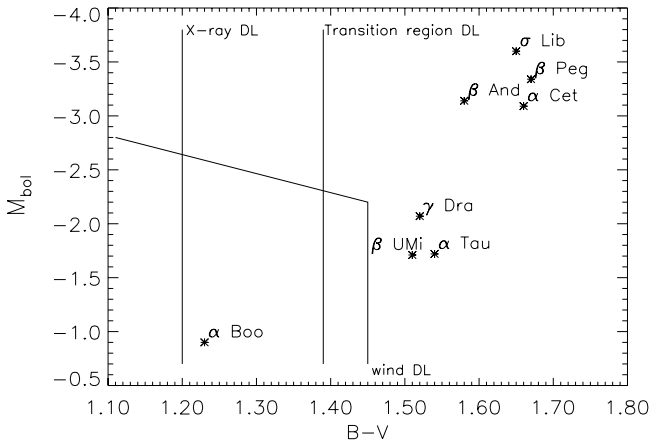

Fig. 4. The position of the different DLs in the HR diagram, together with the eight luminosity class III giants from our sample. The "X-ray DL" is derived by Hünsch et al. (1996), the "transition region DL" by Haisch et al. (1990), and the "wind DL" by Reimers et al. (1996) (see text for more details).

only. Ayres et al. (1981) attempted to observe soft X-ray emission from late-type stars, being a signature of stellar coronae ($T > 10^6$ K). They found an "X-ray DL" roughly coinciding with the "transition region DL" from Linsky & Haisch (1979); only stars to the blue side were detected in X-rays. Stencel & Mullan (1980) studied the morphology of Mg II h and k resonance lines and they also found a similar distinction in position in the HR-diagram between stars with a low-velocity wind in their chromosphere (to the red side of the line) and stars without (to the blue side).

Since the first discovery of the DLs, several authors have confirmed the dichotomy in late-type giant atmospheres, but more sensitive observations have also revised the location of the different DLs in the HR diagram. Hünsch et al. (1996) place the "X-ray DL" at $B - V = 1.2$ for luminosity class III giants. According to Reimers et al. (1996), the "wind DL" runs vertically at $B - V \approx 1.45$, for $B - V < 1.45$ it runs nearly horizontal to $B - V \approx 1.0$ at $M_{\rm bol} \approx -2.8$. Haisch et al. (1990) found that the latest occurrence of emission lines from C IV or Si IV, indicative of a transition region, occurs at K4 III, corresponding to $B - V = 1.385$ (Gray 1992). This places all of our eight stars with luminosity class III in the category of late-type stars with a chromosphere and a cool wind (see Table 1 and Fig. 4). α Boo, although located to the blue side of the wind DL, is known to posses a cool wind (Ayres et al. 1982) and is regarded as an archetype of a non-coronal star. The K2 II giant ι Aur was detected in X-rays by Reimers et al. (1996) and shows C IV and Si IV emission (Haisch et al. 1990), but also circumstellar Ca II H+K lines (Reimers et al. 1996). It is a so-called "hybrid" giant. Hybrid giants are located to the red (i.e. non-coronal side) of the "transition region DL", but show the existence of both transition region plasma and large mass-loss rates (10^{-9}–10^{-10} $M_\odot$/yr) (Harper 1992).

It should, however, be noted that the distinction between coronal and non-coronal giants is not so clear-cut. In a number of recent articles, evidence is given that all giants show some level of X-ray emission when observed with sufficient sensitivity. On the other hand, all observations confirm the significant drop in X-ray emission around early K spectral type for luminosity class III.

X-ray emission from cool stars is linked to the confinement of hot coronal matter in magnetic structures. An understanding of the origin of these magnetic structures is closely related to the physical explanation for the existence of the DLs, both of which are still under discussion. Most authors seem to agree on the fact that a change in surface magnetic field topology is responsible for the DLs. According to Rosner et al. (1995), the field topology of a red giant changes from a large scale organized and closed configuration binding coronal gas, to a largely open magnetic field giving rise to a massive cool wind, as the star evolves along the RGB from the left of the DLs to the right. The transition in topology is ascribed to a change in the origin of the field: as the stellar rotation drops below a critical value, the spin-catalyzed dynamo gives way to a field generation mechanism requiring fluid turbulence as found in the convection zone. It has also been suggested that the magnetic flux tubes that rise up from underneath the convection zone to the stellar surface where they form large scale coronal loops, become trapped in the convective envelope as the convection zone deepens to the right of the DLs (Holzwarth & Schüssler 2001). However, Ayres et al. (1997, 2003) have found evidence in "non-coronal" giants that coronal loops can still rise to the stellar surface: the loops extend beyond the cold molecular layer just above the stellar photosphere, but are at least partially submerged in the chromosphere/COmosphere, where the coronal X-rays are attenuated by overlying material. It is also still unclear if stars evolving along the RGB cross the DLs (as was a.o. postulated by Rosner et al. 1995), or if the evolution tracks run parallel to them (Hünsch et al. 1996). In this last scenario, the difference in X-ray activity on either side of the DLs would be due to a different rotational history of each star implying a difference in spin-catalysed dynamo strength.

In the following sections we will investigate if the observed flux excess in the (sub)millimetre and centimetre wavelength ranges in our selected late-type giants can be explained by a chromosphere (corona) and/or by thermal emission from an ionised stellar wind. As we shall show in Sects. 6.3 and 6.4, the radiation coming from a chromosphere or from an ionised wind exhibits a different frequency dependence $F_\nu \propto \nu^\alpha$. The spectral indices α as determined from the available observations will be compared to the theoretical predictions to determine the cause of the flux excess.

6.3. Thermal emission from an ionised wind

Stars with an ionised wind emit an excess of continuum emission at long wavelengths, i.e. from the IR to the radio region, in addition to the black body flux emission. This excess flux is due to free-free emission or Bremsstrahlung from the wind. To derive the wavelength dependence of the thermal emission from an ionised wind, we will use a model from Olnon (1975). This article gives analytic expressions for the flux originating from a stellar wind, assuming a homogeneous, spherical geometry with a uniform electron temperature and with H II as the only constituent. In reality, the hydrogen in the winds of these late-type stars will be only partially ionised (Drake et al. 1987). The free-free absorption coefficient per unit mass $\kappa_\nu^{\rm ff}$ in cm^2 g^{-1} of an ionised gas at long wavelengths is (e.g. Lamers & Cassinelli 1999)

$$\kappa_\nu^{\rm ff} = 1.78 \times 10^{-2}\, Z^2\, \nu^{-2}\, g_\nu\, T^{-3/2}\, \frac{n_{\rm i}\, n_{\rm e}}{\rho} \qquad (2)$$

where Z^2 is the square of the charge of the atoms, $n_{\rm e}$ and $n_{\rm i}$ are the electron and ion densities in cm^{-3}, ρ is the density in g cm^{-3}

and g_ν is the gaunt factor which will be approximated by a power law

$$g_\nu \simeq 1.37\, T^{0.135}\, \lambda^{0.084} \tag{3}$$

where λ is expressed in centimetre. It is clear from these expressions that the wavelength dependence of the emitted flux will be the same, regardless of the main contributor to the flux, be it H$^-$ ff or H I ff.

Model V from Olnon (1975), the truncated power law distribution is of particular intrest here. It assumes an electron density distribution with a homogeneous sphere in its centre: $n_e \propto r^{-2}$ for $r \geq R$, for $r \leq R$ n_e is constant. Using Eq. (2) in his expressions, the model predicts $F_\nu \propto \nu^{0.611}$ in the optically thick limit and $F_\nu \propto \nu^{-0.084}$ in the optically thin limit. These approximations can be generalised to density distributions $n_e \propto r^{-\beta}$ with $\beta > 1.5$. A value for β differing from 2 can be caused by a non-constant velocity distribution in the wind. This is a very plausible explanation if the radio emission originates from the wind acceleration zone. A decreasing (increasing) fractional ionisation rate (this is the number of free electrons per neutral hydrogen atom) with radius can also lead to a higher (lower) value for β. An extreme case of this scenario would be the existence of an outer cutoff radius r_0 to the ionised portion of the wind. Although doubtful for the targets in our study, this cutoff might be caused for example by the formation of dust at this location in the wind, "quenching" the ionised material (Drake & Linsky 1986). The spectral index would change for $\nu < \nu_0$, where ν_0 is determined by the cutoff radius. For K to mid M cool wind giants, most estimates of the dust-formation region (if present at all) indicate $r_0/R_* \approx 10$. It can be shown that the spectrum is only influenced by this transition for $\lambda \gtrsim 30$ cm (Drake & Linsky 1986). No observations beyond this wavelength are being used in this article, hence such a spatial restriction of the ionised region is of no importance for our discussion.

In the optically thin case the wavelength dependence is not influenced by the value for β. In the optically thick case we have

$$F_\nu \propto \nu^\alpha \quad \text{with} \quad \alpha = \frac{2\beta - 3.084}{\beta - 0.5}. \tag{4}$$

For $\beta = 1.5$ we find $\alpha = -0.084$, which is the same frequency dependence as in the optically thin case. α goes asymptotically to 2 as $\beta \to +\infty$, but we do expect β to fluctuate around 2.

6.4. Chromospheric emission

The continuum radiation from a chromosphere will be mainly free-free emission from H$^-$ and H I. The flux can be written as

$$F_\lambda = \kappa_\lambda^{\rm ff} \rho B_\lambda(T) V \tag{5}$$

in the optically thin case, where V is the volume of the emitting region and B_λ is the Planck function. This expression can be derived from Eq. (1) in Olnon (1975), see also Skinner & Whitmore (1987). With the use of Eq. (2) and the Rayleigh-Jeans approximation for the Planck function where $B_\lambda(T) \propto \lambda^{-4}$, we find a wavelength dependence of $F_\lambda \propto \lambda^{-1.916}$. In case of an optically thick chromosphere, we are looking at a black body with a temperature equal to the electron temperature at the layer where $\tau_\lambda = 1$. In that case we find $F_\lambda \propto \lambda^{-4}$. In the above approximations, the chromosphere is treated as a homogeneous region, with uniform densities and electron temperature.

The model above is also applicable to thermal emission from a corona. This implies that the same wavelength dependence will be found for corona and chromosphere and that our analysis will not allow to discriminate between these two sources of free-free emission.

6.5. Spectral indices for our program stars

Figure 5 shows the true flux excess (the theoretically calculated flux is already subtracted from the data) at millimetre/centimetre wavelengths. We have chosen to plot $\lambda^4 F_\lambda$ in function of wavelength on a logarithmic scale, since the data then follow a horizontal line in case of an optically thick chromosphere. To determine the spectral indices, we searched for the best fitting line through our data using a least-square method. The starting point for these lines coincides with the first wavelength where a flux excess is noticeable (see Sect. 5.2). The spectral index was determined both with and without the upperlimits included. Table 7 summarises which spectral indices are expected for a chromosphere and for an ionised wind based on the simplified analytic expressions derived above.

The least-squares fits for α Cet and β Peg have slopes of ~1.2. This value lies closest to the spectral index expected for an optically thick ionised wind, with β equal to 2.2. For β And, α Tau, β UMi and α Boo, the values for the slope are around 0.8. These values lie somewhere in between the slope of an optically thick ionised wind and an optically thick chromosphere. For ι Aur the three flux values in excess of the model are quite different and do not allow us to have a good fit to the data. Including the upper limits, a slope of 0.80 is derived.

For all stars except ι Aur and α Boo, the least-square fits are made to data at wavelengths longer than 1.2 mm, because only from this wavelength onwards a flux excess was detectable. In these cases, an optically thick ionised wind is the most likely explanation for the observed excess, although the density distributions sometimes show quite large deviations from the average $n_e \propto r^{-2}$. The only star where an optically thick chromosphere is seen, the hybrid giant ι Aur, has a line fitted only to wavelengths shorter than 1.2 mm, because the flux excess was already present in this region and no measurements at longer wavelengths were available. We therefore propose that at shorter wavelengths ($\lambda \lesssim 1$ mm) an optically thick chromosphere is being sampled and at longer wavelengths the continuum forming layers lie further outwards in the atmosphere and the observations show an optically thick ionised wind. It is very well possible that for wavelengths slightly longer than ~1 mm, the optically thick chromosphere is still visible, as this would explain the deviating values for β in the optically thick ionised winds.

7. Conclusions

In seven out of the nine K- and M-giants examined, a clear flux excess at millimetre and/or centimetre wavelengths was found, for the other two targets only observational upper limits are available at centimetre wavelengths. The selected stars have low chromospheric and coronal activity and three of them do belong to the group of so-called "quiet" K- and M-giants, where the near-infrared CO $\Delta v = 1$ lines indicate that the CO-cooled regions, as predicted by radiative equilibrium models, dominate over the chromosphere at altitudes between $\sim 10^{-1/2}$ and 10^{-2} g/cm^2 in mass column density. On the basis of this study, it seems that for these stars the homogeneous atmosphere models based on radiative equilibrium are able to reproduce the CO spectrum around 4.6 μm, but clearly fail to reproduce the flux at millimetre and centimetre wavelengths. At these far-IR wavelengths, a chromosphere and ionised stellar wind cause a clear flux excess.

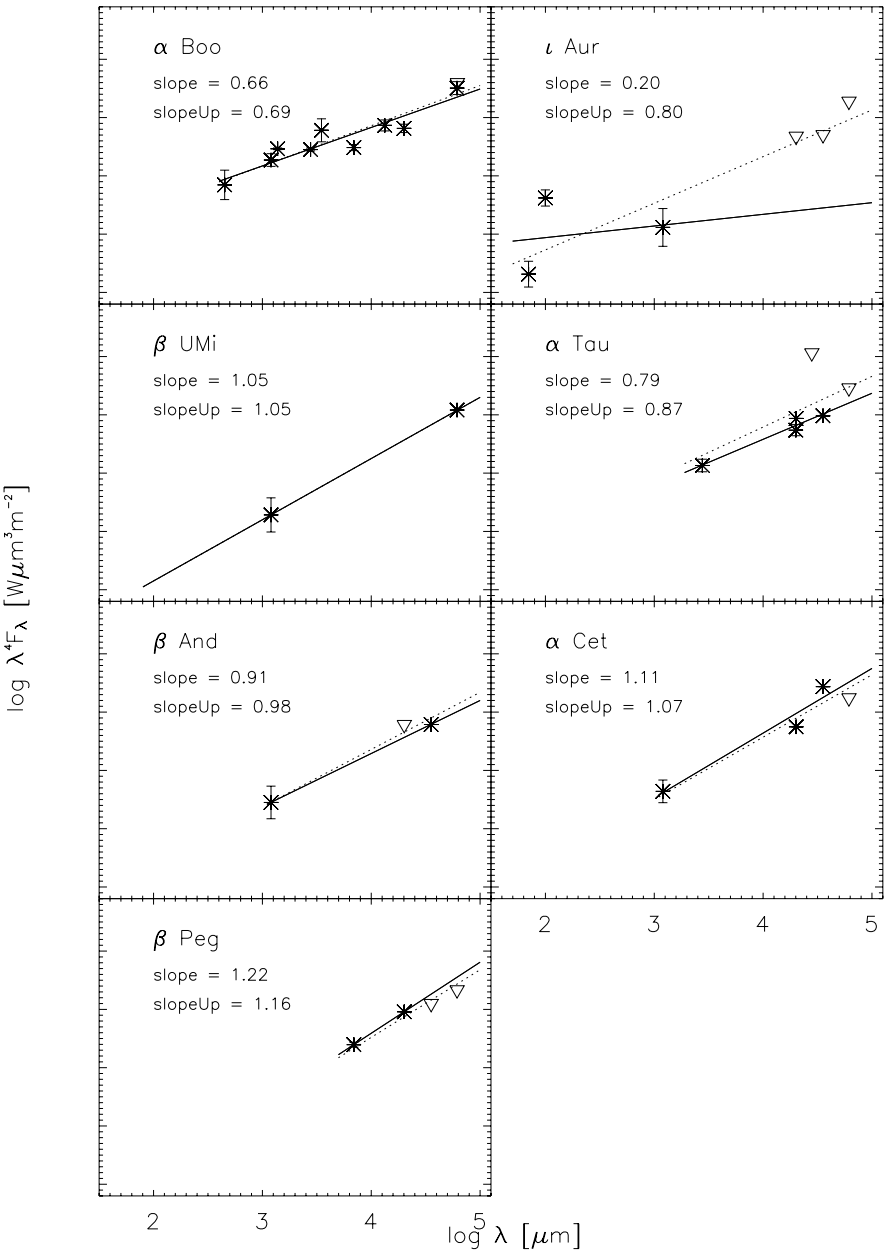

Fig. 5. Flux excess for the seven stars in our sample for which a clear flux excess is detected (i.e. γ Dra and σ Lib are excluded, since only upper limits are available). The observations (with the continuum already subtracted) are represented by asterisks. The lines show the linear least-squares fit to the data. In case of several measurements at one wavelength, the fluxes were replaced by a weighted average. Error bars are shown, but they often fall within the symbols for the fluxes. A triangle represents an upper limit. The full line is a fit to the data points excluding the upper limits. The slope of this fit is indicated by "slope". The dashed line is a fit to the data points including the upper limits to demonstrate the influence of these points on the conclusions. The slope for this fit is indicated by "slopeUp".

Table 7. Summary of the wavelength dependencies of the flux derived for simplified models for the chromosphere and the ionised wind.

	Optically thin	Optically thick
chromosphere	$\lambda^4 F_\lambda \propto \lambda^{2.1}$	$\lambda^4 F_\lambda \propto \lambda^0$
ionised wind	$\lambda^4 F_\lambda \propto \lambda^{2.1}$	$\lambda^4 F_\lambda \propto \lambda^{1.4}$

Notes. The table gives the wavelength dependence for an optically thick ionised wind with a density distribution $n_e \propto r^{-\beta}$ with $\beta = 2$. For $\beta = 1.5$ we have $\lambda^4 F_\lambda \propto \lambda^{2.1}$ and for $\beta \to \infty$ we have $\lambda^4 F_\lambda \propto \lambda^0$.

The observed excess at wavelengths shorter than ~1 mm is most likely to be attributed to an optically thick chromosphere, where an optically thick ionised wind is being sampled at longer wavelengths. The wavelength region where the excess starts depends upon the star under consideration. The most extreme case is ι Aur, where the excess starts somewhere between 60 μm and 100 μm. These findings have implications for the roles of this standard star as fiducial calibrator for PACS (wavelengths between 60 and 210 μm) and SPIRE (between 200 and 670 μm). For α Boo the flux excess is already present at the SPIRE (but not at the PACS) wavelengths. For α Cet it might be present at SPIRE wavelengths and for β And the excess might already start at the PACS wavelengths, but a lack of observations in these regions makes it impossible to indicate the precise start of the excess. α Tau, β Peg, β UMi, γ Dra and σ Lib show no flux excess in the PACS and SPIRE ranges, but especially for σ Lib, only few observations are available in the relevant region. ι Aur shows a clear flux excess from 100 μm onward, and should not be used as a calibrator beyond 60 μm.

Acknowledgements. This work is based on observations collected at the European Southern Observatory, La Silla, Chile within program ESO 71.D-0600 and on observations collected with the IRAM 30 m telescope within project 038_03. We would like to thank R. Zylka and S. Leon for their support for the data reduction. The research at the Caltech Submillimetre Observatory is supported by grant AST-0540882 from the National Science Foundation. S.D. and L.D. acknowledge financial support from the Fund for Scientific Research - Flanders (Belgium). We thank B. Vandenbussche for fruitful discussions.

References

Absil, O., di Folco, E., Mérand, A., et al. 2006, A&A, 452, 237
Aoki, W., & Tsuji, T. 1997, A&A, 328, 175
Arenou, F., Grenon, M., & Gomez, A. 1992, A&A, 258, 104
Ayres, T. R., Linsky, J. L., Vaiana, G. S., Golub, L., & Rosner, R. 1981, ApJ, 250, 293
Ayres, T. R., Simon, T., & Linsky, J. L. 1982, ApJ, 263, 791
Ayres, T. R., Brown, A., Harper, G. M., et al. 1997, ApJ, 491, 876
Ayres, T. R., Brown, A., & Harper, G. M. 2003, ApJ, 598, 610
Beichman, C. A., Neugebauer, G., Habing, H. J., Clegg, P. E., & Chester, T. J. 1988, Infrared astronomical satellite (IRAS) catalogs and atlases, Explanatory supplement, 1
Bell, K. L., & Berrington, K. A. 1987, J. Phys. B At. Mol. Phys., 20, 801
Cohen, M., Walker, R. G., Barlow, M. J., & Deacon, J. R. 1992, AJ, 104, 1650
Cohen, M., Walker, R. G., Carter, B., et al. 1999, AJ, 117, 1864
Cohen, M., Carbon, D., Welch, W., et al. 2005, AJ, 129, 2836
Decin, L. 2000, Ph.D. Thesis, Catholique University of Leuven Department of Physics and Astronomy
Decin, L., & Eriksson, K. 2007, A&A, 472, 1041
Decin, L., Vandenbussche, B., Waelkens, C., et al. 2003a, A&A, 400, 709
Decin, L., Vandenbussche, B., Waelkens, C., et al. 2003b, A&A, 400, 679
Decin, L., Vandenbussche, B., Waelkens, C., et al. 2003c, A&A, 400, 695
Decin, L., Morris, P. W., Appleton, P. N., et al. 2004, ApJS, 154, 408
Dehaes, S., Groenewegen, M. A. T., Decin, L., et al. 2007, MNRAS, 377, 931
Drake, S. A., & Linsky, J. L. 1986, AJ, 91, 602
Drake, S. A., Linsky, J. L., & Elitzur, M. 1987, AJ, 94, 1280
Ducati, J. R. 2002, VizieR Online Data Catalog, 2237, 0
Eggen, O. J., & Stokes, N. R. 1970, ApJ, 161, 199
Gordon, K. D., Engelbracht, C. W., Fadda, D., et al. 2007, PASP, 119, 1019
Gray, D. F. 1992, The Observation and Analysis of Stellar Photospheres ed. D. F. Gray, (Cambridge, UK: Cambridge University Press), 470
Griffin, M. J., & Orton, G. S. 1993, Icarus, 105, 537
Gustafsson, B., Bell, R. A., Eriksson, K., & Nordlund, A. 1975, A&A, 42, 407
Haisch, B. M., Bookbinder, J. A., Maggio, A., Vaiana, G. S., & Bennett, J. O. 1990, ApJ, 361, 570
Harper, G. M. 1992, MNRAS, 256, 37
Holzwarth, V., & Schüssler, M. 2001, A&A, 377, 251
Hünsch, M., Schmitt, J. H. M. M., Schroeder, K.-P., & Reimers, D. 1996, A&A, 310, 801
Jenness, T., Stevens, J. A., Archibald, E. N., et al. 2002, MNRAS, 336, 14
Judge, P. G., & Stencel, R. E. 1991, ApJ, 371, 357
Kashyap, V., Rosner, R., Harnden, Jr., F. R., et al. 1994, ApJ, 431, 402
Lamers, H. J. G. L. M., & Cassinelli, J. P. 1999, Introduction to Stellar Winds (Cambridge University Press)
Linsky, J. L., & Haisch, B. M. 1979, ApJ, 229, L27
Mauas, P. J., Avrett, E. H., & Loeser, R. 1990, ApJ, 357, 279
McWilliam, A. 1990, ApJS, 74, 1075
Morel, M., & Magnenat, P. 1978, A&AS, 34, 477
Obrien, Jr., G. T., & Lambert, D. L. 1986, ApJS, 62, 899
Ochsenbein, F., & Halbwachs, J. L. 1999, VizieR Online Data Catalog, 5053, 0
Olnon, F. M. 1975, A&A, 39, 217
Plez, B., Brett, J. M., & Nordlund, A. 1992, A&A, 256, 551
Poglitsch, A., Waelkens, C., Geis, N., et al. 2010, A&A, 518, L2
Reimers, D., Hünsch, M., Schmitt, J. H. M. M., & Toussaint, F. 1996, A&A, 310, 813
Rosner, R., Musielak, Z. E., Cattaneo, F., Moore, R. L., & Suess, S. T. 1995, ApJ, 442, L25
Rufener, F. 1989, A&AS, 78, 469
Sandell, G. 1994, MNRAS, 271, 75
Selby, M. J., Hepburn, I., Blackwell, D. E., et al. 1988, A&AS, 74, 127
Skinner, C. J., & Whitmore, B. 1987, MNRAS, 224, 335
Skrutskie, M. F., Cutri, R. M., Stiening, R., et al. 2006, AJ, 131, 1163
Smith, B., Price, S., & Baker, R. 2004, ApJS, 154, 673
Stencel, R. E., & Mullan, D. J. 1980, ApJ, 238, 221
Tsuji, T. 1991, A&A, 245, 203
Van Malderen, R., Decin, L., Kester, D., et al. 2004, A&A, 414, 677
Wedemeyer-Böhm, S., & Steffen, M. 2007, A&A, 462, L31
Wendker, H. J. 1995, A&AS, 109, 177
Wiedemann, G., Ayres, T. R., Jennings, D. E., & Saar, S. H. 1994, ApJ, 423, 806
Wright, E. L. 1976, ApJ, 210, 250

Pages 13 to 17 are available in the electronic edition of the journal at http://www.aanda.org

Appendix A: Summary of the photometric data used in this study

Table A.1. Photometric data used in this study for the targets α Boo and ι Aur.

α Boo				ι Aur			
λ [μm]	λF_λ [Wm^{-2}]	error λF_λ [Wm^{-2}]	ref.	λ [μm]	λF_λ [Wm^{-2}]	error λF_λ [Wm^{-2}]	ref.
3.46×10^{-1}	1.22×10^{-9}	1.77×10^{-11}	4	3.46×10^{-1}	4.49×10^{-11}	2.48×10^{-13}	4
3.60×10^{-1}	1.62×10^{-9}	–	1	3.60×10^{-1}	6.23×10^{-11}	–	1
4.01×10^{-1}	4.37×10^{-9}	6.35×10^{-11}	4	4.01×10^{-1}	2.05×10^{-10}	1.13×10^{-12}	4
4.23×10^{-1}	7.40×10^{-9}	9.27×10^{-11}	4	4.23×10^{-1}	4.12×10^{-10}	1.70×10^{-12}	4
4.40×10^{-1}	1.02×10^{-8}	–	1	4.40×10^{-1}	6.20×10^{-10}	–	1
4.48×10^{-1}	1.08×10^{-8}	1.57×10^{-10}	4	4.48×10^{-1}	6.48×10^{-10}	3.58×10^{-12}	4
5.39×10^{-1}	2.02×10^{-8}	2.93×10^{-10}	4	5.39×10^{-1}	1.55×10^{-9}	8.55×10^{-12}	4
5.49×10^{-1}	2.15×10^{-8}	2.18×10^{-10}	4	5.49×10^{-1}	1.69×10^{-9}	3.12×10^{-12}	4
5.50×10^{-1}	2.17×10^{-8}	–	1	5.50×10^{-1}	1.74×10^{-9}	–	1
5.81×10^{-1}	2.48×10^{-8}	3.60×10^{-10}	4	5.81×10^{-1}	2.02×10^{-9}	1.12×10^{-11}	4
7.00×10^{-1}	3.30×10^{-8}	–	1	7.00×10^{-1}	2.88×10^{-9}	–	1
7.00×10^{-1}	3.33×10^{-8}	–	6	9.00×10^{-1}	3.84×10^{-9}	–	1
9.00×10^{-1}	3.77×10^{-8}	–	1	1.24	3.98×10^{-9}	6.89×10^{-10}	12
9.00×10^{-1}	3.81×10^{-8}	–	6	1.25	3.31×10^{-9}	–	1
1.24	3.08×10^{-8}	4.45×10^{-9}	12	1.25	3.40×10^{-9}	–	6
1.25	2.88×10^{-8}	–	1	1.66	3.51×10^{-9}	4.91×10^{-10}	12
1.25	3.28×10^{-8}	–	6	2.16	2.01×10^{-9}	2.93×10^{-10}	12
1.24	2.82×10^{-8}	2.41×10^{-10}	2	2.20	1.53×10^{-9}	–	1
2.16	1.35×10^{-8}	2.11×10^{-9}	12	2.20	1.60×10^{-9}	3.43×10^{-11}	7
2.20	1.30×10^{-8}	–	1	3.40	5.65×10^{-10}	–	1
2.20	1.39×10^{-8}	1.53×10^{-10}	7	3.50	5.30×10^{-10}	1.82×10^{-11}	7
2.21	1.48×10^{-8}	1.36×10^{-10}	14	3.50	4.83×10^{-10}	1.82×10^{-11}	7
3.40	4.92×10^{-9}	–	1	5.00	1.65×10^{-10}	–	1
3.40	4.83×10^{-9}	–	1	1.02×10^{1}	4.34×10^{-11}	–	1
3.50	4.33×10^{-9}	1.03×10^{-10}	7	1.02×10^{1}	3.81×10^{-11}	–	6
3.50	4.02×10^{-9}	1.03×10^{-10}	7	1.20×10^{1}	1.54×10^{-11}	3.07×10^{-12}	3
3.77	3.52×10^{-9}	2.86×10^{-10}	14	2.50×10^{1}	1.76×10^{-12}	3.53×10^{-13}	3
4.74	1.54×10^{-9}	1.54×10^{-11}	14	6.00×10^{1}	1.36×10^{-13}	2.73×10^{-14}	3
5.00	1.65×10^{-9}	–	1	1.00×10^{2}	6.66×10^{-14}	1.33×10^{-14}	3
5.00	1.68×10^{-9}	–	6	1.20×10^{3}	3.25×10^{-17}	7.50×10^{-18}	5
8.78	3.01×10^{-10}	3.01×10^{-12}	14	1.20×10^{3}	1.37×10^{-17}	4.50×10^{-18}	10
9.91	2.21×10^{-10}	–	14	2.01×10^{4}	$<6.13 \times 10^{-20}$	–	5
1.02×10^{1}	1.60×10^{-10}	–	1	3.55×10^{4}	$<1.18 \times 10^{-20}$	–	5
1.02×10^{1}	2.38×10^{-10}	–	6	6.14×10^{4}	$<8.31 \times 10^{-21}$	–	5
1.16×10^{1}	1.34×10^{-10}	1.34×10^{-12}	14				
1.20×10^{1}	1.39×10^{-10}	2.79×10^{-11}	3				
1.24×10^{1}	1.13×10^{-10}	–	14				
2.50×10^{1}	1.39×10^{-11}	2.78×10^{-12}	3				
6.00×10^{1}	9.79×10^{-13}	1.96×10^{-13}	3				
1.00×10^{2}	2.17×10^{-13}	4.35×10^{-14}	3				
3.50×10^{2}	4.53×10^{-15}	7.19×10^{-16}	13				
4.50×10^{2}	2.94×10^{-15}	4.46×10^{-16}	13				
1.20×10^{3}	2.64×10^{-16}	4.17×10^{-17}	9				
1.20×10^{3}	1.95×10^{-16}	2.00×10^{-17}	5				
1.38×10^{3}	1.82×10^{-16}	3.72×10^{-18}	8				
2.77×10^{3}	2.18×10^{-17}	7.48×10^{-19}	8				
3.49×10^{3}	1.84×10^{-17}	6.45×10^{-18}	5				
6.92×10^{3}	1.45×10^{-18}	8.23×10^{-20}	11				
6.92×10^{3}	1.43×10^{-18}	1.73×10^{-19}	11				
1.33×10^{4}	$<1.12 \times 10^{-17}$	–	5				
1.33×10^{4}	3.82×10^{-19}	6.74×10^{-20}	11				
2.00×10^{4}	1.02×10^{-19}	1.35×10^{-20}	5				
2.80×10^{4}	$<1.07 \times 10^{-18}$	–	5				
6.14×10^{4}	1.91×10^{-20}	6.35×10^{-21}	5				
6.14×10^{4}	1.27×10^{-20}	2.44×10^{-21}	5				
6.17×10^{4}	$<1.75 \times 10^{-20}$	–	5				

Notes. The literature references are specified at the end of Table A.5.

Table A.2. Photometric data used in this study for the targets β UMi and γ Dra.

β UMi				γ Dra			
λ [μm]	λF_λ [Wm^{-2}]	error λF_λ [Wm^{-2}]	ref.	λ [μm]	λF_λ [Wm^{-2}]	error λF_λ [Wm^{-2}]	ref.
3.46×10^{-1}	8.12×10^{-11}	8.73×10^{-13}	4	3.46×10^{-1}	5.58×10^{-11}	4.45×10^{-13}	4
3.60×10^{-1}	1.17×10^{-10}	–	1	3.60×10^{-1}	8.84×10^{-11}	–	1
4.01×10^{-1}	3.91×10^{-10}	4.19×10^{-12}	4	4.01×10^{-1}	2.99×10^{-10}	2.38×10^{-12}	4
4.23×10^{-1}	7.79×10^{-10}	7.17×10^{-12}	4	4.23×10^{-1}	6.17×10^{-10}	4.02×10^{-12}	4
4.40×10^{-1}	1.15×10^{-9}	–	1	4.40×10^{-1}	9.65×10^{-10}	–	1
4.48×10^{-1}	1.24×10^{-9}	1.33×10^{-11}	4	4.48×10^{-1}	1.01×10^{-9}	8.04×10^{-12}	4
5.39×10^{-1}	2.78×10^{-9}	2.99×10^{-11}	4	5.39×10^{-1}	2.35×10^{-9}	1.88×10^{-11}	4
5.49×10^{-1}	3.01×10^{-9}	2.22×10^{-11}	4	5.49×10^{-1}	2.57×10^{-9}	1.18×10^{-11}	4
5.50×10^{-1}	3.06×10^{-9}	–	1	5.50×10^{-1}	2.69×10^{-9}	–	1
5.81×10^{-1}	3.66×10^{-9}	3.93×10^{-11}	4	5.81×10^{-1}	3.19×10^{-9}	2.54×10^{-11}	4
7.00×10^{-1}	5.28×10^{-9}	–	1	7.00×10^{-1}	4.77×10^{-9}	–	1
9.00×10^{-1}	6.68×10^{-9}	–	1	9.00×10^{-1}	6.56×10^{-9}	–	1
1.24	6.10×10^{-9}	1.09×10^{-9}	12	1.24	4.84×10^{-9}	9.46×10^{-10}	12
1.25	6.43×10^{-9}	–	6	1.25	6.37×10^{-9}	–	6
1.25	5.64×10^{-9}	2.01×10^{-10}	7	1.25	5.46×10^{-9}	2.20×10^{-10}	7
1.66	5.82×10^{-9}	9.86×10^{-10}	12	1.25	5.29×10^{-9}	1.23×10^{-10}	2
2.16	3.03×10^{-9}	5.68×10^{-10}	12	1.65	5.38×10^{-9}	–	14
2.20	3.09×10^{-9}	–	6	1.66	4.88×10^{-9}	8.09×10^{-10}	12
2.20	2.85×10^{-9}	3.32×10^{-11}	7	2.16	2.70×10^{-9}	3.97×10^{-10}	12
3.50	9.18×10^{-10}	2.94×10^{-11}	7	2.16	3.02×10^{-9}	–	14
3.50	8.69×10^{-10}	2.94×10^{-11}	7	2.20	2.97×10^{-9}	–	6
1.20×10^{1}	2.82×10^{-11}	5.65×10^{-12}	3	2.20	2.80×10^{-9}	4.24×10^{-11}	7
2.50×10^{1}	3.26×10^{-12}	6.52×10^{-13}	3	2.21	3.09×10^{-9}	4.92×10^{-11}	14
6.00×10^{1}	2.17×10^{-13}	4.35×10^{-14}	3	3.40	1.09×10^{-9}	–	1
1.00×10^{2}	5.73×10^{-14}	1.15×10^{-14}	3	3.40	1.03×10^{-9}	–	6
1.20×10^{3}	4.00×10^{-17}	1.00×10^{-17}	5	3.50	9.18×10^{-10}	2.45×10^{-11}	7
1.20×10^{3}	3.05×10^{-17}	6.00×10^{-18}	10	3.50	8.69×10^{-10}	2.45×10^{-11}	7
6.14×10^{4}	5.37×10^{-21}	–	5	3.65	8.11×10^{-10}	–	14
				3.77	7.42×10^{-10}	6.67×10^{-11}	14
				5.00	3.23×10^{-10}	–	6
				8.78	6.02×10^{-11}	9.88×10^{-13}	14
				9.91	4.66×10^{-11}	–	14
				1.02×10^{1}	3.81×10^{-11}	–	1
				1.02×10^{1}	3.88×10^{-11}	–	1
				1.20×10^{1}	2.72×10^{-11}	5.45×10^{-12}	3
				1.24×10^{1}	2.36×10^{-11}	–	14
				2.50×10^{1}	3.24×10^{-12}	6.48×10^{-13}	3
				6.00×10^{1}	2.25×10^{-13}	4.51×10^{-14}	3
				1.00×10^{2}	4.89×10^{-14}	9.77×10^{-15}	3
				3.50×10^{2}	9.94×10^{-16}	2.57×10^{-16}	3
				1.20×10^{3}	2.52×10^{-17}	5.00×10^{-18}	10
				1.20×10^{3}	$<3.00 \times 10^{-17}$	–	5
				2.01×10^{4}	$<6.42 \times 10^{-20}$	–	5
				3.55×10^{4}	$<1.27 \times 10^{-20}$	–	5

Notes. The literature references are specified at the end of Table A.5.

Table A.3. Photometric data used in this study for the targets α Tau and β And.

α Tau				β And			
λ [μm]	λF_λ [Wm^{-2}]	error λF_λ [Wm^{-2}]	ref.	λ [μm]	λF_λ [Wm^{-2}]	Error λF_λ [Wm^{-2}]	ref.
3.46×10^{-1}	1.85×10^{-10}	3.51×10^{-12}	4	3.46×10^{-1}	5.38×10^{-11}	6.61×10^{-13}	4
3.60×10^{-1}	2.93×10^{-10}	–	1	3.60×10^{-1}	9.17×10^{-11}	–	1
4.01×10^{-1}	9.98×10^{-10}	1.90×10^{-11}	4	4.01×10^{-1}	3.11×10^{-10}	3.83×10^{-12}	4
4.23×10^{-1}	2.09×10^{-9}	3.47×10^{-11}	4	4.23×10^{-1}	6.60×10^{-10}	5.98×10^{-12}	4
4.40×10^{-1}	3.31×10^{-9}	–	1	4.40×10^{-1}	1.08×10^{-9}	–	1
4.48×10^{-1}	3.37×10^{-9}	6.40×10^{-11}	4	4.48×10^{-1}	1.07×10^{-9}	1.31×10^{-11}	4
5.39×10^{-1}	8.08×10^{-9}	1.53×10^{-10}	4	5.39×10^{-1}	2.72×10^{-9}	3.34×10^{-11}	4
5.49×10^{-1}	8.79×10^{-9}	1.21×10^{-10}	4	5.49×10^{-1}	2.94×10^{-9}	1.08×10^{-11}	4
5.50×10^{-1}	9.41×10^{-9}	–	1	5.50×10^{-1}	3.14×10^{-9}	–	1
5.81×10^{-1}	1.07×10^{-8}	2.04×10^{-10}	4	5.81×10^{-1}	3.59×10^{-9}	4.41×10^{-11}	4
7.00×10^{-1}	1.81×10^{-8}	–	1	7.00×10^{-1}	6.12×10^{-9}	–	1
9.00×10^{-1}	2.71×10^{-8}	–	1	9.00×10^{-1}	9.65×10^{-9}	–	1
1.24	2.66×10^{-8}	4.75×10^{-9}	12	1.24	9.33×10^{-9}	1.77×10^{-9}	12
1.25	2.31×10^{-8}	–	1	1.25	8.68×10^{-9}	2.92×10^{-10}	7
1.25	2.38×10^{-8}	–	6	1.25	9.20×10^{-9}	–	6
1.25	2.18×10^{-9}	4.85×10^{-10}	2	1.25	8.35×10^{-9}	1.91×10^{-10}	2
1.66	2.43×10^{-8}	3.80×10^{-9}	12	1.66	8.80×10^{-9}	1.20×10^{-9}	12
2.16	1.53×10^{-8}	1.97×10^{-9}	12	2.16	5.06×10^{-9}	7.46×10^{-10}	12
2.20	1.14×10^{-8}	–	1	2.20	4.83×10^{-9}	5.64×10^{-11}	7
2.20	1.19×10^{-8}	–	6	2.20	3.92×10^{-9}	–	6
2.21	1.30×10^{-8}	2.08×10^{-10}	14	2.21	5.14×10^{-9}	8.20×10^{-11}	14
3.40	4.33×10^{-9}	–	6	3.40	1.87×10^{-9}	–	1
3.50	3.79×10^{-9}	9.27×10^{-11}	7	3.40	1.74×10^{-9}	–	6
3.50	3.65×10^{-9}	9.27×10^{-11}	7	3.50	1.56×10^{-9}	3.78×10^{-11}	7
3.77	3.22×10^{-9}	2.64×10^{-10}	14	3.50	1.45×10^{-9}	3.78×10^{-11}	7
4.74	1.27×10^{-9}	3.70×10^{-11}	14	3.77	1.30×10^{-9}	1.06×10^{-10}	14
5.00	1.24×10^{-9}	–	1	4.74	4.93×10^{-10}	1.46×10^{-11}	14
5.00	1.40×10^{-9}	–	6	5.00	4.75×10^{-10}	–	1
8.78	2.65×10^{-10}	4.27×10^{-12}	14	5.00	5.51×10^{-10}	–	6
1.02×10^{1}	1.52×10^{-10}	–	1	8.78	1.06×10^{-10}	1.72×10^{-12}	14
1.02×10^{1}	1.95×10^{-10}	–	6	1.02×10^{1}	6.94×10^{-11}	–	1
1.16×10^{1}	1.23×10^{-10}	1.99×10^{-12}	14	1.02×10^{1}	8.11×10^{-11}	–	6
1.20×10^{1}	1.23×10^{-10}	2.46×10^{-11}	3	1.16×10^{1}	4.98×10^{-11}	8.21×10^{-13}	14
2.50×10^{1}	1.31×10^{-11}	2.61×10^{-12}	3	1.20×10^{1}	5.05×10^{-11}	1.01×10^{-11}	3
2.74×10^{1}	9.55×10^{-12}	2.64×10^{-12}	8	2.50×10^{1}	5.84×10^{-12}	1.17×10^{-12}	3
6.00×10^{1}	9.79×10^{-13}	1.96×10^{-13}	3	6.00×10^{1}	4.08×10^{-13}	8.16×10^{-14}	3
1.00×10^{2}	1.76×10^{-13}	3.52×10^{-14}	3	1.00×10^{2}	8.39×10^{-14}	1.68×10^{-14}	3
3.50×10^{2}	4.54×10^{-15}	7.02×10^{-19}	13	1.20×10^{3}	6.25×10^{-17}	1.00×10^{-17}	5
4.50×10^{2}	2.03×10^{-15}	4.00×10^{-16}	13	1.20×10^{3}	5.87×10^{-17}	6.85×10^{-18}	10
1.20×10^{3}	1.27×10^{-16}	1.50×10^{-17}	5	1.20×10^{3}	$<1.00 \times 10^{-16}$	–	9
1.38×10^{3}	5.62×10^{-17}	1.23×10^{-17}	8	1.33×10^{4}	$<2.02 \times 10^{-17}$	–	5
2.77×10^{3}	1.51×10^{-17}	1.58×10^{-18}	8	2.01×10^{4}	8.37×10^{-20}	–	5
2.00×10^{4}	8.98×10^{-20}	1.50×10^{-20}	5	2.80×10^{4}	$<5.34 \times 10^{-19}$	–	5
2.01×10^{4}	1.28×10^{-19}	–	5	3.55×10^{4}	1.52×10^{-20}	–	5
2.80×10^{4}	$<5.34 \times 10^{-19}$	–	5	6.14×10^{4}	$<1.03 \times 10^{-20}$	–	5
3.55×10^{4}	2.53×10^{-20}	–	5	6.97×10^{5}	$<4.30 \times 10^{-19}$	–	5
6.14×10^{4}	$<1.32 \times 10^{-20}$	–	5				
6.97×10^{5}	$<4.30 \times 10^{-19}$	–	5				

Notes. The literature references are specified at the end of Table A.5.

Table A.4. Photometric data used in this study for the targets α Cet and β Peg.

α Cet				β Peg			
λ [μm]	λF_λ [Wm^{-2}]	error λF_λ [Wm^{-2}]	ref.	λ [μm]	λF_λ [Wm^{-2}]	error λF_λ [Wm^{-2}]	ref.
3.46×10^{-1}	3.44×10^{-11}	5.67×10^{-13}	4	3.46×10^{-1}	3.36×10^{-11}	1.80×10^{-12}	4
3.60×10^{-1}	5.68×10^{-11}	–	1	3.60×10^{-1}	5.95×10^{-11}	–	6
4.01×10^{-1}	1.98×10^{-10}	3.27×10^{-12}	4	3.60×10^{-1}	6.23×10^{-11}	–	1
4.23×10^{-1}	4.16×10^{-10}	5.70×10^{-12}	4	4.01×10^{-1}	2.16×10^{-10}	1.16×10^{-11}	4
4.40×10^{-1}	6.49×10^{-10}	–	1	4.23×10^{-1}	4.42×10^{-10}	2.32×10^{-11}	4
4.48×10^{-1}	6.82×10^{-10}	1.13×10^{-11}	4	4.40×10^{-1}	6.99×10^{-10}	–	6
5.39×10^{-1}	1.82×10^{-9}	3.00×10^{-11}	4	4.40×10^{-1}	6.61×10^{-10}	–	1
5.49×10^{-1}	1.98×10^{-9}	2.01×10^{-11}	4	4.48×10^{-1}	7.17×10^{-10}	3.84×10^{-11}	4
5.50×10^{-1}	2.02×10^{-9}	–	1	5.39×10^{-1}	2.01×10^{-9}	1.07×10^{-10}	4
5.81×10^{-1}	2.39×10^{-9}	3.95×10^{-11}	4	5.49×10^{-1}	2.15×10^{-9}	1.11×10^{-10}	4
7.00×10^{-1}	4.35×10^{-9}	–	1	5.50×10^{-1}	2.24×10^{-9}	–	6
9.00×10^{-1}	7.95×10^{-9}	–	1	5.50×10^{-1}	2.08×10^{-9}	–	1
1.24	7.51×10^{-9}	9.90×10^{-10}	12	5.81×10^{-1}	2.53×10^{-9}	1.36×10^{-10}	4
1.25	7.11×10^{-9}	–	1	7.00×10^{-1}	5.53×10^{-9}	–	6
1.25	7.56×10^{-9}	2.40×10^{-10}	7	7.00×10^{-1}	5.48×10^{-9}	–	1
1.66	8.27×10^{-9}	1.39×10^{-9}	12	9.00×10^{-1}	1.17×10^{-8}	–	6
2.20	3.85×10^{-9}	–	1	9.00×10^{-1}	1.15×10^{-8}	–	1
2.20	4.10×10^{-9}	4.63×10^{-11}	7	1.24	1.45×10^{-8}	2.58×10^{-9}	12
3.40	1.36×10^{-9}	–	1	1.25	1.20×10^{-8}	4.31×10^{-10}	7
3.40	1.53×10^{-9}	–	1	1.25	1.10×10^{-8}	4.31×10^{-10}	7
3.50	1.33×10^{-9}	4.36×10^{-11}	7	1.25	1.10×10^{-8}	1.34×10^{-10}	2
3.50	1.26×10^{-9}	4.36×10^{-11}	7	1.66	1.34×10^{-8}	2.22×10^{-9}	12
5.00	3.64×10^{-10}	–	1	2.16	8.27×10^{-9}	1.17×10^{-9}	12
5.00	4.58×10^{-10}	–	6	2.20	6.51×10^{-9}	–	1
1.02×10^{1}	5.17×10^{-11}	–	1	2.20	6.98×10^{-9}	9.16×10^{-11}	7
1.02×10^{1}	6.10×10^{-11}	–	6	2.21	7.43×10^{-9}	9.52×10^{-11}	14
1.20×10^{1}	4.12×10^{-11}	8.24×10^{-12}	3	3.40	2.42×10^{-9}	–	1
2.50×10^{1}	4.78×10^{-12}	9.57×10^{-13}	3	3.40	2.56×10^{-9}	–	1
6.00×10^{1}	3.38×10^{-13}	6.76×10^{-14}	3	3.50	2.25×10^{-9}	5.76×10^{-11}	7
1.00×10^{2}	6.69×10^{-14}	1.34×10^{-14}	3	3.50	2.09×10^{-9}	5.76×10^{-11}	7
3.50×10^{2}	1.80×10^{-15}	3.08×10^{-16}	13	3.77	1.92×10^{-9}	1.57×10^{-10}	14
4.50×10^{2}	7.33×10^{-16}	2.20×10^{-16}	13	4.74	7.11×10^{-10}	2.07×10^{-11}	14
1.20×10^{3}	3.75×10^{-17}	7.50×10^{-18}	5	5.00	7.26×10^{-10}	–	1
1.20×10^{3}	1.46×10^{-16}	2.33×10^{-17}	9	5.00	8.26×10^{-10}	–	6
2.01×10^{4}	7.62×10^{-20}	–	5	8.78	1.55×10^{-10}	2.50×10^{-12}	14
3.55×10^{4}	6.25×10^{-20}	–	5	1.02×10^{1}	9.94×10^{-11}	–	1
3.56×10^{4}	$<1.43 \times 10^{-18}$	–	5	1.02×10^{1}	1.24×10^{-10}	–	6
6.14×10^{4}	$<7.82 \times 10^{-21}$	–	5	1.16×10^{1}	7.15×10^{-11}	1.16×10^{-12}	14
1.31×10^{5}	$<1.01 \times 10^{-18}$	–	5	1.20×10^{1}	6.82×10^{-11}	1.36×10^{-11}	3
				2.50×10^{1}	8.29×10^{-12}	1.66×10^{-12}	3
				6.00×10^{1}	5.95×10^{-13}	1.19×10^{-13}	3
				1.00×10^{2}	1.03×10^{-13}	2.06×10^{-14}	3
				3.50×10^{2}	3.09×10^{-15}	3.17×10^{-16}	13
				4.50×10^{2}	1.60×10^{-15}	1.80×10^{-16}	13
				1.20×10^{3}	5.75×10^{-17}	1.25×10^{-17}	5
				1.20×10^{3}	7.29×10^{-17}	1.22×10^{-17}	9
				1.20×10^{3}	7.37×10^{-17}	1.37×10^{-17}	10
				7.00×10^{3}	1.07×10^{-18}	5.14×10^{-20}	11
				2.01×10^{4}	1.25×10^{-19}	–	5
				3.55×10^{4}	$<3.04 \times 10^{-20}$	–	5
				6.14×10^{4}	$<9.77 \times 10^{-21}$	–	5

Notes. The literature references are specified at the end of Table A.5.

Table A.5. Photometric data used in this study for σ Lib.

σ Lib			
λ [μm]	λF_λ [Wm^{-2}]	error λF_λ [Wm^{-2}]	ref.
3.46×10^{-1}	1.62×10^{-11}	5.96×10^{-13}	4
3.60×10^{-1}	2.82×10^{-11}	–	6
3.60×10^{-1}	2.62×10^{-11}	–	1
4.01×10^{-1}	9.69×10^{-11}	3.57×10^{-12}	4
4.23×10^{-1}	1.98×10^{-10}	6.70×10^{-12}	4
4.40×10^{-1}	3.08×10^{-10}	–	1
4.40×10^{-1}	3.28×10^{-10}	–	6
4.48×10^{-1}	3.24×10^{-10}	1.19×10^{-11}	4
5.39×10^{-1}	9.09×10^{-10}	3.35×10^{-11}	4
5.49×10^{-1}	9.77×10^{-10}	2.97×10^{-11}	4
5.50×10^{-1}	1.02×10^{-9}	–	1
5.50×10^{-1}	1.08×10^{-9}	–	6
5.81×10^{-1}	1.16×10^{-9}	4.26×10^{-11}	4
7.00×10^{-1}	2.60×10^{-9}	–	1
7.00×10^{-1}	2.96×10^{-9}	–	6
9.00×10^{-1}	5.35×10^{-9}	–	1
9.00×10^{-1}	5.98×10^{-9}	–	6
1.24	5.19×10^{-9}	7.84×10^{-10}	12
1.25	5.65×10^{-9}	–	6
1.25	5.20×10^{-9}	1.40×10^{-10}	7
1.66	5.70×10^{-9}	9.13×10^{-10}	12
2.16	3.35×10^{-9}	6.12×10^{-10}	12
2.20	3.21×10^{-9}	4.88×10^{-11}	6
2.20	3.09×10^{-9}	4.88×10^{-11}	7
3.40	1.18×10^{-9}	–	1
3.50	1.00×10^{-9}	2.52×10^{-11}	7
3.50	9.46×10^{-10}	2.52×10^{-11}	7
5.00	3.23×10^{-10}	–	1
5.00	3.60×10^{-10}	–	6
1.02×10^{1}	3.51×10^{-11}	–	1
1.02×10^{1}	4.42×10^{-11}	–	6
1.20×10^{1}	3.55×10^{-11}	7.10×10^{-12}	3
2.50×10^{1}	3.69×10^{-12}	7.39×10^{-13}	3
6.00×10^{1}	3.00×10^{-13}	6.00×10^{-14}	3
1.00×10^{2}	6.84×10^{-14}	1.37×10^{-14}	3
1.20×10^{3}	3.02×10^{-17}	6.75×10^{-18}	10
3.57×10^{4}	$<4.54 \times 10^{-19}$	–	5
6.14×10^{4}	$<1.03 \times 10^{-20}$	–	5

References. (1) UBVRIJKLMNH Photoelectric Catalogue (Morel & Magnenat 1978). (2) Selby et al. (1988). (3) IRAS catalogue of Point Sources, Version 2.0. (4) Observations in the Geneva Photometric System 4 (Rufener 1989). (5) Radio continuum emission from stars (Wendker 1995). (6) Stellar Photometry in Johnson's 11-color system (Ducati 2002). (7) Color corrected data from COBE DIRBE Point Source Catalog (Smith et al. 2004). (8) Cohen et al. (2005). (9) Dehaes et al. (2007). (10) IRAM observations (this article). (11) VLA observations (this article). (12) 2MASS All-Sky Catalog of Point Sources (Skrutskie et al. 2006). (13) CSO observations (this article). (14) Ground-based and KAO data from M. Cohen et al. for the ISO CWW absolute calibration programme.